RSC Advances

PAPER

View Article Online
View Journal | View Issue

Cite this: *RSC Adv.*, 2020, **10**, 39981

Heterogeneous synthesis and electrochemical performance of $LiMnPO_4$/C composites as cathode materials of lithium ion batteries†

Ju-Gong Zheng, *[a] Guang-Yuan Ren,[a] Jun Shi,[a] Ting Yang,*[a] Yue-Feng Tang[b] and Yan-Feng Chen[b]

In this study, a facile yet efficient interfacial hydrothermal process was successfully developed to fabricate $LiMnPO_4$/C composites. In this strategy, the walls of carbon nanotubes were employed as heterogeneous nucleation interfaces and biomass of phytic acid (PA) as an eco-friendly phosphorus source. By comparing the experimental results, a reasonable nucleation-growth mechanism was proposed, suggesting the advantages of interfacial effects. Meanwhile, the as-synthesized $LiMnPO_4$/C samples exhibited superior rate performances with discharge capacities reaching 161 mA h g^{-1} at C/20, 134 mA h g^{-1} at 1C, and 100 mA h g^{-1} at 5C. The composites also displayed excellent cycling stabilities by maintaining 95% of the initial capacity over 100 continuous cycles at 1C. Electrochemical impedance spectroscopy showed that the superior electrochemical performances were attributed to the low charge-transfer resistance and elevated diffusion coefficient of lithium ions. In sum, the proposed approach for the preparation of $LiMnPO_4$/C composites looks promising for future production of composite electrode materials for high-performance lithium-ion batteries.

Received 28th September 2020
Accepted 27th October 2020

DOI: 10.1039/d0ra08274k

rsc.li/rsc-advances

1. Introduction

Over the past few decades, rechargeable lithium-ion batteries (LIBs) have widely been used as eco-friendly power sources in portable electronics and large applications, such as electric vehicles and energy storage devices, thanks to their high energy density, long cycle life and good safety.[1,2] The current depleting energy resources and the pollution crisis have encouraged the development of clean power sources based on LIBs. One way to achieve this is through the synthesis of high performance materials[3,4] as the core component of LIBs, in which cathode materials could directly affect the electrochemical performance and desirable eco-friendliness of the batteries. In recent years, tremendous efforts have been devoted to the development of LIBs materials, such as $LiMPO_4$ (M = Mn, Fe) and $LiMPO_4$ to replace cobalt oxide ($LiCoO_2$) cathode materials used in commercial LIBs with relatively high toxicity, poor thermal stability, and high cost.[1,2,5–7] So far, $LiMnPO_4$ is the most promising cathode material for high energy systems[8,9] but still suffers from high-current discharge, limiting its extensive applications.[10]

Therefore, numerous modification strategies have been utilized to enhance its electrochemical performances, including improvement of particle dispersion and grain refinement by various synthetic techniques,[6,11,12] use of ion doping and solid solution,[9,13,14] and coating with electronically conducting agents.[15–17] Among these, the hydrothermal strategy is widely adopted for homogeneous synthesis due to its mild operating conditions, non-toxicity, and environmental protection.[10] However, $LiMnPO_4$ primary grains are keen on rearranging and stacking along certain directions, leading to the assembly of secondary structures in hydrothermal systems.[18–22] The building blocks would inhibit enhanced kinetics and high specific capacity. Therefore, well-dispersed primary particles are urgently expected in the synthesis process.

The rearrangement habits of $LiMnPO_4$ grains are determined by its preferential growth direction. The preferential growth depends on the polarity and energy of the crystal plane.[23] In the crystal lattice of $LiMnPO_4$, the polarity of crystal plane is closely related to the areal density of atoms.[24] Besides, the interface energy of (100), (010) and (001) planes in $LiMnPO_4$ are differently influenced by the presence of additives and the heterogeneous nucleation interfaces are different.[25] Therefore, the addition of additives and the use of heterogeneous nucleation systems could inevitably influence the structure and morphology of $LiMnPO_4$. Wang Y. *et al.*[26] reported a solvothermal synthesis of $LiMnPO_4$/C composites using hexade-cyltrimethylammonium bromide

[a]*Fundamental Science on Radioactive Geology and Exploration Technology Laboratory, East China University of Technology, 418 Guanglan Avenue, Nanchang, Jiangxi, 330013, China. E-mail: jgzheng@ecut.edu.cn; yt1551@126.com; Fax: +86-791-83896550; Tel: +86-791-83896550*

[b]*National Laboratory of Solid State Microstructures, Nanjing University, 22 Hankou Road, Nanjing, Jiangsu,210093, China*

† Electronic supplementary information (ESI) available. See DOI: 10.1039/d0ra08274k

(CTAB) as a surfactant. The authors determined that the morphology is mainly dependant on the amount of CTAB. M. K. Devaraju *et al.*[10] introduced the effects of additives and surfactants on crystal size and morphology of $LiMnPO_4$ nanocrystals in the presence of ascorbic acid. The decrease in particle size to less than 100 nm could be more effective in electrochemical reactions because nanoparticles provide short lengths for lithium ion diffusion during the charge/discharge process. Jing S. *et al.*[27] reported a solvothermal synthesis of $LiMnPO_4$ employing poly(vinyl pyrrolidone) (PVP) as the additive. The as-synthesized $LiMnPO_4$ microstructures exhibit unique, well-shaped and favorable structures, which are self-assembled from microplates or microrods. The *b* axis is the preferred crystal growth orientation of the products, resulting in a shorter lithium ion diffusion path.

A facile hydrothermal strategy to synthesis well dispersed $LiMnPO_4$ particles was developed by using phytic acid (PA) as phosphorus source. Ethanol, polyethylene glycol and carbon nanotubes were introduced into the ethanol or water to form heterogeneous nucleation system. The heterogeneous nucleation reaction system is highly desired to decrease particle size and increase dispersion of primary particles. The well dispersed $LiMnPO_4$ particles will reduce the Li^+ migration length and improve the kinetics of $LiMnPO_4$. As-obtained $LiMnPO_4$/C composites do show a high reversible specific capacity of 158 mA h g^{-1} at 0.1C, as well as the superior high-rate capability and excellent cycling stability.

2. Experimental

2.1 Synthesis of $LiMnPO_4$ *via* homogeneous nucleation

In a typical synthesis, 2 mmol PA (Aladdin Chemistry Co., Ltd., 50%) and 36 mmol $LiOH \cdot H_2O$ (Alfa Aesar, 98%) were successively dissolved in distilled water under stirring vigorously for 30 min to obtain a brownish yellow transparent solution. Afterward, 12 mmol $MnSO_4 \cdot 7H_2O$ (Sigma-Aldrich, 98%) aqueous solution was added to the above obtained brownish yellow solution under magnetic stirring and high-purity nitrogen continuous stream at room temperature for 30 min. Then the mixture was quickly transferred into a 100 mL Teflon-lined stainless-steel autoclave, heated at 180 °C for 6 h, and then naturally cooled to ambient temperature. The as-obtained precipitates were collected by centrifugation and followed by washing several times with distilled water and ethanol, and finally drying in an oven at 60 °C under air atmosphere for 10 h. To determine the appropriate calcination temperatures, the as-prepared precursors were characterized by thermogravimetry and differential scanning calorimetry (TG-DSC, STA449F1, NETZSCH, Germany). The as-prepared precursors were finally transferred to a tube furnace and calcined under a mixed atmosphere of Ar (90%) and H_2 (10%). The resulting products were denoted as PA–LMP.

2.2 Synthesis of $LiMnPO_4$/C composites *via* heterogeneous nucleation

First, 300 mg carbon nanotubes (Shenzhen Nanotech Port Co. Ltd, L-MWNT-10-20, outer diameter is about 10–20 nm, length > 5 μm, purity > 75%) were dispersed in 150 mL distilled water to yield a uniform suspension. Next, 36 mmol $MnSO_4 \cdot 7H_2O$ were added to the suspension under magnetic stirring to form a heterogeneous nucleation system, which then was divided into three equal volumes for subsequent experiments. Meanwhile, three parts of 2 mmol PA and three portions of 36 mmol $LiOH \cdot H_2O$ were separately dissolved into 30 mL distilled water, 30 mL ethanol/water and 30 mL PEG600/water to obtain three mixed solutions. Finally, three mixed solutions were severally dripped into the three heterogeneous nucleation systems with magnetic stirring to yield three different mixtures, which then were quickly transferred into a 100 mL Teflon-lined stainless-steel autoclave followed by reactions, washing, collection, drying and calcination as PA–LMP. The resulting products from water solvent suspension system were denoted as PA–LMP/C, those from ethanol/water solvent suspension system were named as ethanol–PA–LMP/C, and products issued from PEG600/water solvent suspension system were called PEG–PA–LMP/C.

2.3 Cells assembly and electrochemical measurement

The fabrication of cathodes and assembly process of CR2032-type coin cells are provided in the ESI (Section I†). The electrochemical performances of $LiMnPO_4$/C composites were evaluated by galvanostatic cycling using CR2032-type coin cells. The charge/discharge performances were collected on battery and cell equipment (Maccor S4000, USA) at different current densities in the voltage range of 2.5–4.5 V *vs.* Li^+/Li. Electrochemical impedance spectroscopy (EIS) was carried out on the electrochemical work station (AUTOLAB PGSTAT30, Metrohm Ltd, Switzerland) over the frequency range of 100 kHz to 0.01 Hz and alternating voltage of 5 mV. All electrochemical measurements were performed in CR2032-type coin cells at room temperature.

3. Results and discussion

3.1 TG-DSC analysis

The TG-DSC curves of the precursor are presented in Fig. S1.† The TG curve consisted of three stages with the first two stages showing two obvious weight losses attributed to the dehydration and decomposition of the organic components. In the third stage, an endothermic peak appeared at 550 °C and mainly due to the formation of crystalline phase.[28] Almost no weight loss and no thermal effect were observed above 600 °C, indicating the absence of thermal decomposition. Therefore, a calcination temperature of 600 °C was selected and used as optimal value for the preparation of $LiMnPO_4$ materials.

3.2 Products prepared *via* homogeneous nucleation

3.2.1 Structure and morphology. The FT-IR absorption spectra of the precursor and the calcined product are gathered in Fig. S2, and detailed analyses are provided in the ESI.† The absorption spectra of the precursor and calcined product both showed the presence of PO_4 group. No considerable shift in the absorption band was observed, indicating the incorporation of

manganese ions in PA to successfully form a stable olivine-type structure due to the high negative charges on the surface.[29,30]

The XRD patterns of products prepared by homogeneous nucleation are presented in Fig. 1. The precursor (Fig. 1a) and calcined product PA–LMP (Fig. 1b) both confirmed the presence of single-phase $LiMnPO_4$ with olivine structure indexed to orthorhombic (JCPDS 74-0375). Moreover, the relative intensities of the characteristic peaks of PA–LMP looked overall higher and more easily indexed than those of precursor. The partial enlargement of two patterns shows the characteristic peaks appeared at16.9° and 29.2° corresponding to (020) and (200) crystal planes. The peak width (FWHM) and the peak intensity of PA–LMP are higher than those of the precursor. Thus, the crystallinities of the products improved by the calcination process.

The SEM and TEM images of products prepared from homogeneous nucleation are shown in Fig. 2. The precursor was mainly composed of boat-shaped micro-ellipsoid with major diameters ranging from 3 to 5 μm (Fig. 2a and b). An HRTEM image of a single $LiMnPO_4$ micro-ellipsoid is provided in Fig. 2c. The building blocks were assembled by many nanoparticles side by side in an ordered mode. The fringe spacing value was estimated to about 0.523 nm, consistent with the (020) crystal plane of orthorhombic phase $LiMnPO_4$ with a *Pnma* space group. Most PA–LMP particles retained their original morphologies, even though scattering of a few primary grains occurred (Fig. 2d). The scattering phenomenon was related to carbonized products. In other words, organic components among the granules can be carbonized during the calcination process, leading to loosing or even separating of tiny blocks. As shown in Fig. 2e and f, the surface of each particle was coated with an unevenly distributed carbon layer. The existence of trace carbon in PA–LMP sample could be attributed to the carbon rings in PA molecules. The amount of carbon in PA–LMP sample determined by elemental analysis was about 1.7 wt%.

3.2.2 Charge/discharge profiles. The initial charge–discharge profiles of two cells assembled with the precursor and PA–LMP as cathode materials are exhibited in Fig. 3. The charge/discharge profiles of PA–LMP showed an obvious plateau accompanying a tolerable polarization of 210 mV and smaller specific energy loss, consistent with the high coulombic efficiency shown in section I. The first charge/discharge capacity are 152 and 126 mA h^{-1} respectively, and the coulomb efficiency is about 83%. By comparison, the cell assembled with the precursor delivered a high-intensive polarization and a poor coulombic efficiency verified in section II. The first charge/discharge capacity are 133 and 77 mA h^{-1} respectively, and the coulomb efficiency is about 58%. Also, PA–LMP sample presented a much higher initial discharge specific capacity than the precursor, suggesting the advantages of PA–LMP over the precursor in terms of electrochemical performance.

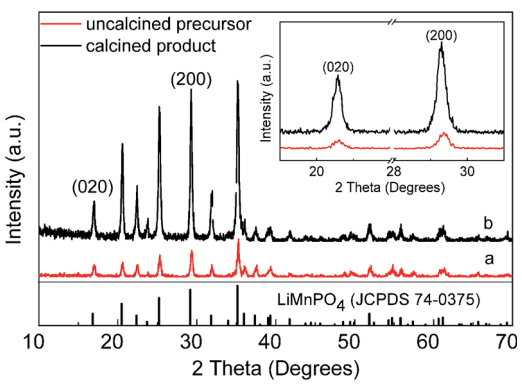

Fig. 1 XRD patterns of the products synthesized *via* homogeneous nucleation along with partial enlargement of XRD patterns (inset). XRD pattern of the precursor (a), XRD pattern of the calcined product PA–LMP (b).

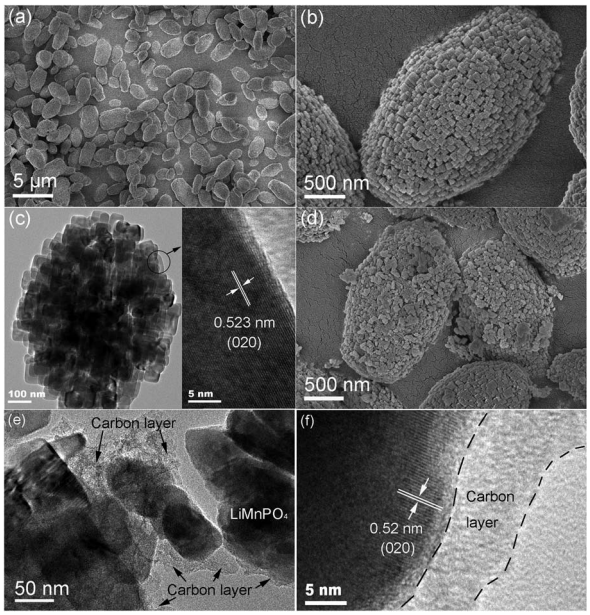

Fig. 2 SEM and TEM images of the as-synthesized products by homogeneous nucleation. (a–c) SEM and TEM images of precursor, (d–f) SEM and TEM images of PA–LMP.

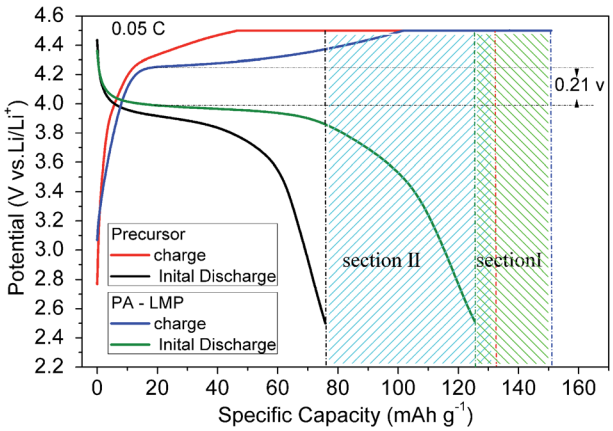

Fig. 3 Initial charge/discharge voltage profiles of two cells assembled with precursor and PA–LMP as cathode materials. Conditions: charged at a constant current rate of 0.05 C–4.5 V, holding at 4.5 V until 0.01 C, and then discharged at a constant current rate of 0.05 C–2.5 V.

3.3 $LiMnPO_4$/C composites synthesized by three heterogeneous nucleation systems

3.3.1 Crystal phases. Comparison between the three heterogeneous nucleation systems were carried out carefully to clarify the best $LiMnPO_4$/C composite consisting of dispersed primary particles and carbon conductive agent. The samples prepared from three suspension solutions were analysed by XRD and the data are displayed in Fig. 4. The presence of three patterns confirmed the presence of single-phase $LiMnPO_4$ with olivine structure indexed to orthorhombic (JCPDS 74-0375). The relative intensities of characteristic peaks of PA–LMP/C looked superior to those of ethanol–PA–LMP/C and PEG–PA–LMP/C. Thus, crystal grains synthesized from the organic solutions were refined and crystallinities decreased. Note that PA–LMP/C, ethanol–PA–LMP/C, and PEG–PA–LMP/C were all prepared using the same dosage (5 wt%) of MWNTs since their contents would influence the electrochemical performances. The carbon contents in PA–LMP/C, ethanol–PA–LMP/C and PEG–PA–LMP/C determined by elemental analysis were about 5.9 wt%, 6.3 wt% and 7.2 wt%, respectively. The carbon content in each sample increased at varying degrees, indicating the contribution of carbon content from organic solvents in addition toMWNTs.

3.3.2 Microstructure. SEM and TEM images of products obtained from three heterogeneous nucleation systems are illustrated in Fig. 5. PA–LMP/C sample exhibited primary particles, secondary particles, and microsphere (Fig. 5a and d). The primary particles and MWNTs were mainly distributed at intervals in local ranges, while no carbon nanotubes were observed in certain areas where primary particles self-assembled into secondary particles. In Fig. 5b and e, ethanol–PA–LMP/C particles appeared relatively uniform and well-dispersed. Nanosized particles were separately distributed in continuous array of MWNTs. PEG–PA–LMP/C sample showed severe aggregations (Fig. 5c and f). Therefore, the microstructures of $LiMnPO_4$/C composites were significantly affected by the heterogeneous nucleation system. In the aqueous solvent suspension system, active atoms easily migrated to the surface

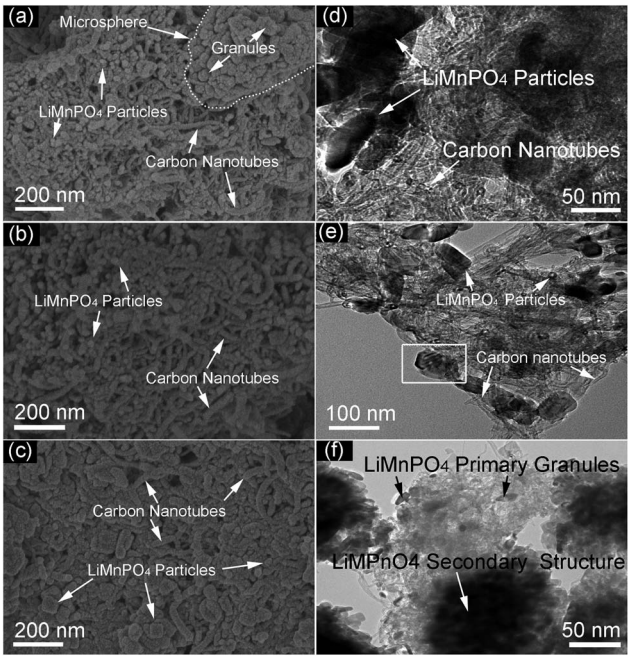

Fig. 5 SEM and TEM images of the products synthesized from heterogeneous nucleation systems. (a and d) PA–LMP/C, (b and e) ethanol–PA–LMP/C, (c and f) PEG–PA–LMP/C.

of the nucleus and grown preferentially into secondary structures owing to the relatively low viscous resistance solution. By contrast, the activation energy and migration energy of surface atoms increased in the organic solvent suspension system, thereby reducing the size of the nucleus and increasing agglomeration.

A possible growth mechanism of ethanol–PA–LMP/C composites was proposed based the structural analysis and the results are schematically illustrated in Fig. 6.

First, PA was fully dissolved in an ethanol–water mixed solvent, and MWNTs were uniformly dispersed in an aqueous solution containing Mn^{2+} ions (Fig. 6, step a). During the initial

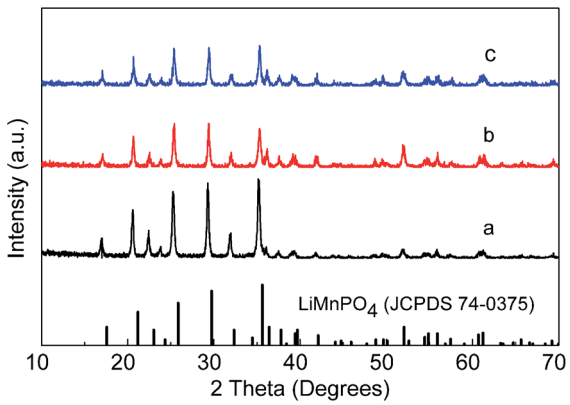

Fig. 4 XRD patterns of the products synthesized from heterogeneous nucleation systems. (a) PA–LMP/C (from water solvent suspension system), (b) ethanol–PA–LMP/C (from ethanol/water solvent suspension system), (c) PEG–PA–LMP/C (from PEG 600/water solvent suspension system).

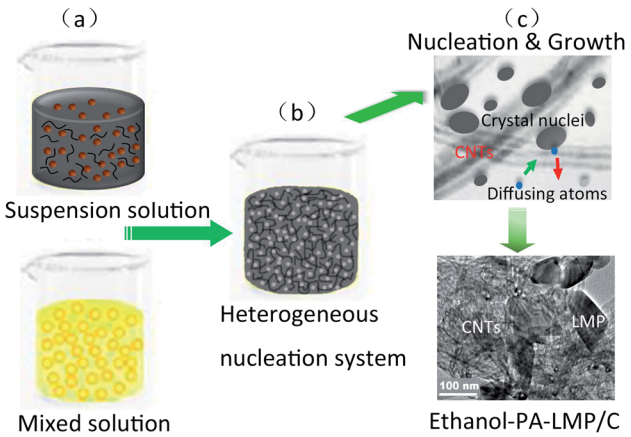

Fig. 6 Schematic illustration for the ethanol/water solvent heterogeneous nucleation process of $LiMnPO_4$/C composites.

step of the hydrothermal process in the heterogeneous system, numerous tiny nuclei were generated and dispersed in solution or adhering to the walls of MWNTs. Thus PA formed homogeneous hydrogen-containing lithium salt, as well as PA cross-linked complexes with Mn^{2+} owing to the chelating (Fig. 6, step b).[29] In following hydrothermal reaction, the atoms diffused from the solution to the nucleus surface, along with the reverse diffusion from the nucleus to solution. A great number of crystal nuclei were generated on the surface of MWNTs thanks to the relative diffusivity and heterogeneous nucleation caused by interfacial effect. On the other hand, the diffusion activation energy of MWNTs–nucleus interface is higher than that of liquid–nucleus interface. Hence, the surface atoms of MWNTs–nucleus interface could not easily overcome the activation barrier, thereby remained bound to the lattice. In the subsequent process, the crystal nucleus continued to grow up (Fig. 6, step c). By contrast, nucleus in the solution tend to dissolution and aggregate due to thermal undulation.[29,31] This led to the assembly of small primary particles with different sizes into secondary microspheres, consistent with the Ostwald ripening theory.[32]

3.3.3 Electrochemical performances. To evaluate the effects of structure on the electrochemical performances, the electrodes in the three cells were charged and discharged at C/20 in the first cycle, then charged at C/10 in the following charging steps while discharged at gradually increasing rates. As shown in Fig. 7a–c, the galvanostatic charge/discharge voltage profiles showed unanimous results. The charge/discharge curves delivered obvious plateaus around 4.1 V and considerable discharge capacities at lower currents. The polarization between the charge/discharge curves obviously deteriorated with the increase in current density, leading to sharply declined discharge specific capacities.[33] By contrast, ethanol–PA–LMP/C exhibited less polarization and superior discharge capacity, with discharge plateau still retained at 3.2 V and the discharge capacity up to 60 mA h g^{-1} at 10C rate. The inferior discharge curves at higher rates were linked to polarization of the cell induced by its internal resistance.[28,34] An appreciable plateau was maintained at around 4.0 V until C/5, reflecting the low internal resistance of ethanol–PA–LMP/C material. The internal resistance of the cells will further be discussed in the later EIS data. The rate capacity of ethanol–PA–LMP/C looked better than two other compounds. Although PA–LMP/C delivered a considerable specific capacity of 150 mA h g^{-1} at C/10, almost no electrochemical activity was obtained at 2C, implying sluggish lithium ion transfer in aggregated PA–LMP/C particles. PEG-PA–LMP/C delivered a discharge capacity below 80 mA h g^{-1} at 2C, lagged far behind ethanol–PA–LMP/C material at high current densities. In Fig. 7d, the cycling performance curves revealed comparable capacity retentions of the three materials at C/10 rate. As discharge current density increased to 1C, the capacity retention rate of PA–LMP/C and PEG–PA–LMP/C significantly reduced, meaning severe deterioration of the cycling stability. Ethanol–PA–LMP/C maintains 97% of initial capacity after 80 cycles at a C/10 and 95% after 100 cycles at 1C. Thus ethanol–PA–LMP/C cathode materials exhibited high specific capacity, superior high-rate capability,

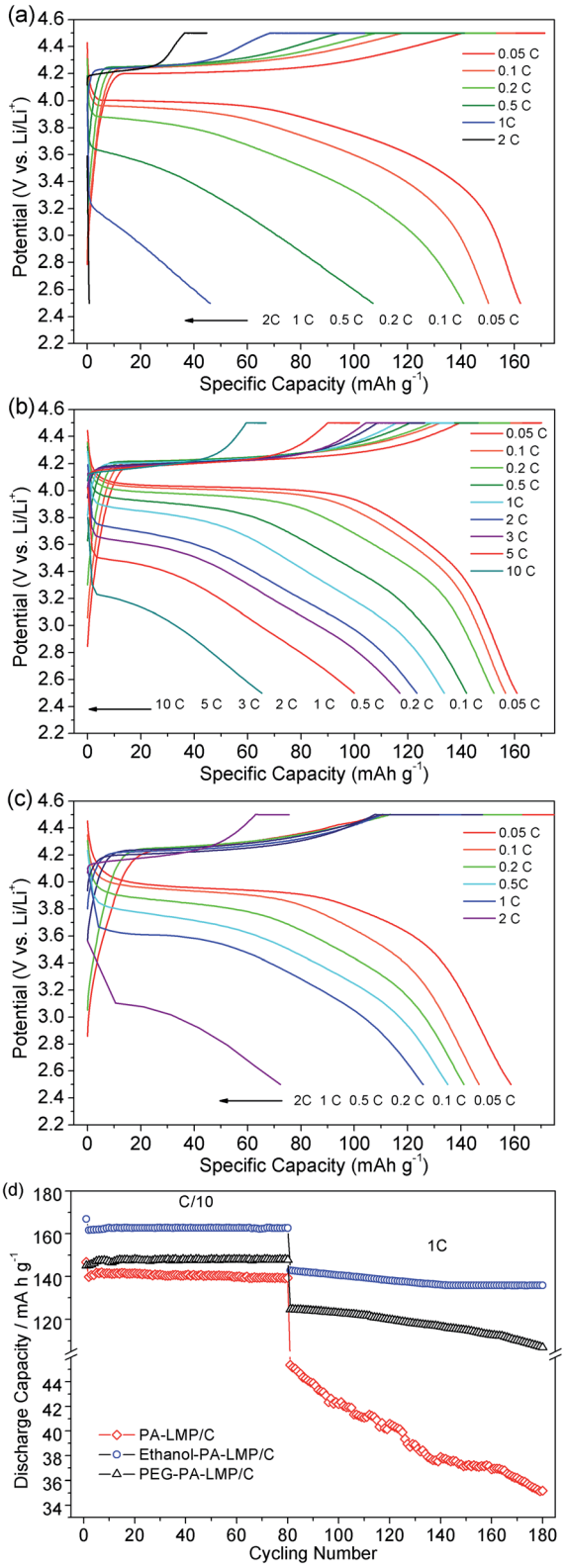

Fig. 7 Charge and discharge profiles of PA–LMP/C (a), ethanol–PA–LMP/C (b), PEG–PA–LMP/C (c) and cycling performances of three $LiMnPO_4$/C composites (d).

and excellent cycling stability. The superior rate capability of ethanol–PA–LMP/C was mainly attributed to the improved electrical conductivity benefiting from the facile diffusion of

lithium ions and fast transport of electrons. The structure of ethanol–PA–LMP/C composites consisted of well-dispersed nanoparticle and continuous conductive carbon. The nanoparticles provide shorter diffusion distance for lithium ions, thereby reducing the time required for lithium ions to embed in $LiMnPO_4$ lattices. Furthermore, continuous conductive carbon would offer three-dimensional networks and barrier-free paths to electronics, which could effectively accelerate the transport of electrons and enhance the electrical conductivity.[2,17] By contrast, the cycling stability of PA–LMP/C and PEG–PA–LMP/C were clearly inferior to that of ethanol–PA–LMP/C. PEG–PA–LMP/C showed severe capacity fading, especially during cycling at 1C rate. The capacity fading may be caused by a continual side reaction.[35,36] The Jahn–Teller distortion of trivalent manganese ions could cause the distortion of electron clouds and volume effects of $LiMnPO_4$ particles. ethanol–PA–LMP/C particles could generally maintain their original structure, owing to the primary structures and high crystalline states. However, PEG–PA–LMP/C particles might crack due to their hierarchical structures and aggregate states, creating new active surface area of $LiMnPO_4$ for the electrolyte infiltration. The Li salt could be possibly consumed by side-reactions occurring at the electrolyte/electrode interface, resulting in slight loss of active material and capacity fading. Furthermore, the rate capability could decrease because of increased bulk resistance stemmed from the decline in Li salt concentration.

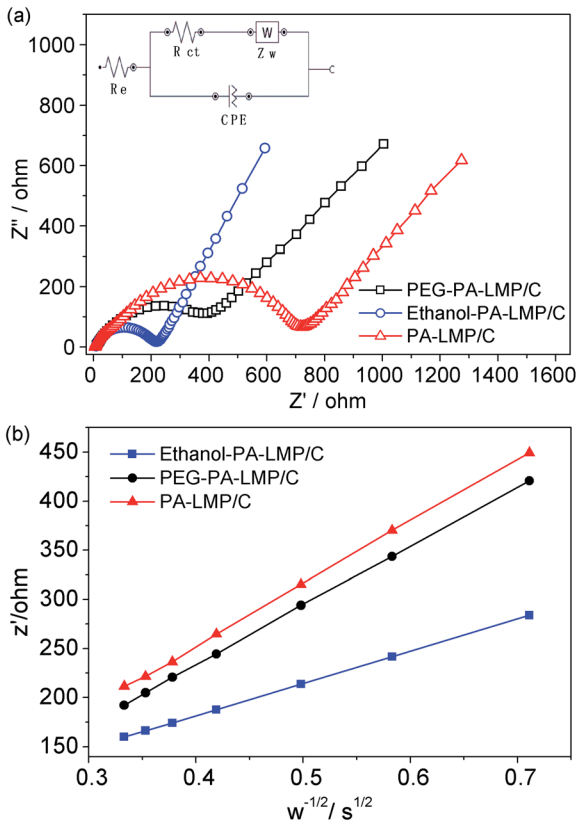

Fig. 8 (a) Impedance spectra of PA–LMP/C, ethanol–PA–LMP/C and PEG–PA–LMP/C after the rate test, and the corresponding equivalent circuit. (b) The plots of the real resistance as a function of the inverse square root of the angular frequency.

To gain a better understanding of the electrochemical behaviors and kinetics of the three $LiMnPO_4$/C composites, electrochemical impedance spectroscopy (EIS) measurements were performed and the data are shown in Fig. 8. The Nyquist plots and corresponding equivalent circuits in Fig. 8a revealed each impedance spectrum composed of one semicircle component in the high-to-medium frequency range and sloping line component at low frequencies. The high frequency part of the semicircle was related to the formation of EIS films on the electrode surface. The medium frequency part corresponds to charge transfer process. The sloping line in the low-frequency range was associated with the Warburg impedance.[37,38] The simulation results estimated the charge-transfer resistance (R_{ct}) values of PA–LMP/C, ethanol–PA–LMP/C and PEG–PA–LMP/C to 274.6, 107.3 and 196.8 Ω, respectively. The EIS of ethanol–PA–LMP/C electrode exhibited a small semicircular domain, indicatingfast charge-transfer process. The charge transfer kinetics were consistent with the superior rate performance and excellent cycling stability.[39,40] The Warburg impedance was related to the diffusion of lithium ions in the electrode. The diffusion coefficients of lithium ions (D_{Li}) were calculated according to the following equation:

$$D = \frac{T^2R^2}{2\sigma^2 n^4 A^2 C^2 F^4}$$

where T is the absolute temperature, R represents the gas constant, σ denotes the Warburg factor, n is the number of electrons per molecule during oxidization, A refers to the surface area of the electrode, C is the concentration of lithium ions and F is the Faraday constant.

As shown in the insert of Fig. 8b, the value of σ represented the slope of the lines between the real resistance (Z') and the inverse square root of the angular frequency ($\omega^{-1/2}$). The D_{Li} values of PA–LMP/C, ethanol–PA–LMP/C and PEG–PA–LMP/C were determined as 1.98×10^{-13}, 8.37×10^{-13} and 3.16×10^{-13} $cm^2\ S^{-1}$, respectively. The diffusion of lithium ions in ethanol–PA–LMP/C was faster than those in PA–LMP/C and PEG–PA–LMP/C. The rapid diffusion can be attributed to the intrinsic structure of ethanol–PA–LMP/C, consisting of primary particles and continuous MWNTs. The nanosized particles shorten the diffusion distance and provide large current for high rate performance.[2,41] In sum, the EIS resultsagree well with the superior electrochemical performance of ethanol–PA–LMP/C.

4. Conclusions

Homogeneous nucleation and heterogeneous nucleation techniquewere employed for the preparation of well-dispersed $LiMnPO_4$/C composites using biomass of phytic acid as phosphorus source. The distribution and microstructure of $LiMnPO_4$ particles can easily be controlled by adjusting the volume ratio of ethanol and dosage of MWNTs. By comparison, $LiMnPO_4$ primary particles prepared by homogeneous nucleation strategy showed apparent aggregations. The products obtained by heterogeneous nucleation system displayed better distribution

due to the heterogeneous nucleation interface of MWNTs. This greatly improved the conductivity and migration rate of Li ions. As a result, ethanol–PA–LMP/C samples exhibited superior rate performances with discharge capacities reaching 100 mA h g^{-1} at 5C, also displayed excellent cycling stabilities by maintaining 95% of the initial capacity over 100 continuous cycles at 1C. Superior rate and excellent cycling performances implies a great potential for use as cathode materials in LIBs. Furthermore, the proposed synthesis strategy could be useful for large-scale synthesis of other materials with eco-friendly and green development aspects.

Conflicts of interest

There are no conflicts to declare.

Acknowledgements

This research was supported by the National Natural Science Foundation of China (No. 51869002), a grant for National Laboratory of Solid State Microstructures (No. M29033), a grant for Fundamental Science on Radioactive Geology and Exploration Technology Laboratory (No. RGET1811), a project funded by Jiangxi New Energy Technology and Equipment Engineering Technology Research Center (JXNE2016-09), a Test Foundation of Nanjing University.

References

1 L. Liang, X. Sun, J. Zhang, L. Hou, J. Sun, Y. Liu, S. Wang and C. Yuan, *Adv. Energy Mater.*, 2019, **9**, 1802847.
2 J. Li, S.-h. Luo, Q. Wang, S. Yan, J. Feng, X. Ding, P. He and L. Zong, *J. Electrochem. Soc.*, 2019, **166**, A118–A124.
3 W. Chen and H. Fang, *J. Electrochem. Soc.*, 2019, **166**, A2752–A2754.
4 K. Zhang, G.-H. Lee, M. Park, W. Li and Y.-M. Kang, *Adv. Energy Mater.*, 2016, **6**, 1600811.
5 V. Ragupathi, P. Panigrahi and G. S. Nagarajan, *Appl. Surf. Sci.*, 2019, **495**, 143541.
6 N. H. Kwon, H. Yin, T. Vavrova, J. H. W. Lim, U. Steiner, B. Grobéty and K. M. Fromm, *J. Power Sources*, 2017, **342**, 231–240.
7 X. Xu, T. Wang, Y. Bi, M. Liu, W. Yang, Z. Peng and D. Wang, *J. Power Sources*, 2017, **341**, 175–182.
8 D. Choi, D. Wang, I. T. Bae, J. Xiao, Z. Nie, W. Wang, V. V. Viswanathan, Y. J. Lee, J. G. Zhang, G. L. Graff, Z. Yang and J. Liu, *Nano Lett.*, 2010, **10**, 2799–2805.
9 V. Aravindan, J. Gnanaraj, Y. S. Lee and S. Madhavi, *J. Mater. Chem. A*, 2013, **1**, 3518–3539.
10 M. K. Devaraju and I. Honma, *Adv. Energy Mater.*, 2012, **2**, 284–297.
11 J. Zheng, C. Qin, T. Wu, S. Xie, L. Ni, M. Peng, Y. Tang and Y. Chen, *J. Mater. Chem. A*, 2015, **3**, 15299–15306.
12 H. J. Zhu, W. Zhai, M. Yang, X. M. Liu, Y. C. Chen, H. Yang and X. D. Shen, *RSC Adv.*, 2014, **4**, 25625–25632.
13 I. Seo, B. Senthilkumar, K.-H. Kim, J.-K. Kim, Y. Kim and J.-H. Ahn, *J. Power Sources*, 2016, **320**, 59–67.
14 D. Y. Wang, C. Y. Ouyang, T. Drezen, I. Exnar, A. Kay, N. H. Kwon, P. Gouerec, J. H. Miners, M. K. Wang and M. Gratzel, *J. Electrochem. Soc.*, 2010, **157**, A225–A229.
15 W. Chen and H. Fang, *J. Electrochem. Soc.*, 2019, **166**, A2752–A2754.
16 J. G. Duan, Y. B. Cao, J. B. Jiang, K. Du, Z. D. Peng and G. R. Hu, *J. Power Sources*, 2014, **268**, 146–152.
17 J. L. Liu, X. Y. Liu, T. Huang and A. S. Yu, *J. Power Sources*, 2013, **229**, 203–209.
18 N. Priyadharsini, A. Shanmugavani, S. Surendran, B. Senthilkumar, L. Vasylechko and R. Kalai Selvan, *J. Mater. Sci.: Mater. Electron.*, 2018, **29**, 18553–18565.
19 J. Zhang, S. Luo, Q. Wang, Z. Wang, A. Hao, Y. Zhang, Y. Liu, Q. Xu and Y. Zhai, *J. Alloys Compd.*, 2017, **701**, 433–438.
20 Z. Gao, X. L. Pan, H. P. Li, S. K. Xie, R. X. Yi and W. Jin, *Crystengcomm*, 2013, **15**, 7808–7814.
21 T. Li, T. Mei, Y. C. Zhu, H. X. Gong, T. Huang and Y. T. Qian, *Chem. Lett.*, 2011, **40**, 837–839.
22 J. F. Ni and L. J. Gao, *J. Power Sources*, 2011, **196**, 6498–6501.
23 L. Bao, Y. Chen, G. Xu, T. Yang and Z. Ji, *Eur. J. Inorg. Chem.*, 2018, **2018**, 1533–1539.
24 D. Z. Chen, W. Wei, R. N. Wang, X. F. Lang, Y. Tian and L. Guo, *Dalton Trans.*, 2012, **41**, 8822–8828.
25 L. Wang, F. Zhou and G. Ceder, *Electrochem. Solid-State Lett.*, 2008, **11**, A94–A96.
26 Y. Wang, Y. Yang, Y. Yang and H. Shao, *Solid State Commun.*, 2010, **150**, 81–85.
27 J. Su, B. Q. Wei, J. P. Rong, W. Y. Yin, Z. X. Ye, X. Q. Tian, L. Ren, M. H. Cao and C. W. Hu, *J. Solid State Chem.*, 2011, **184**, 2909–2919.
28 J. Zheng, L. Ni, Y. Lu, C. Qin, P. Liu, T. Wu, Y. Tang and Y. Chen, *J. Power Sources*, 2015, **282**, 444–451.
29 J. Su, X.-L. Wu, C.-P. Yang, J.-S. Lee, J. Kim and Y.-G. Guo, *J. Phys. Chem. C*, 2012, **116**, 5019–5024.
30 A. Salah, P. Jozwiak, J. Garbarczyk, K. Benkhouja, K. Zaghib, F. Gendron and C. Julien, *J. Power Sources*, 2005, **140**, 370–375.
31 A. Pimpinelli and J. Villain, *Journal*, 1998, 60–69.
32 B. P. Jia and L. Gao, *Cryst. Growth Des.*, 2008, **8**, 1372–1376.
33 A. K. Padhi, K. S. Nanjundaswamy and J. B. Goodenough, *J. Electrochem. Soc.*, 1997, **144**, 1188–1194.
34 L. F. Zhang, Q. T. Qu, L. Zhang, J. Li and H. H. Zheng, *J. Mater. Chem. A*, 2014, **2**, 711–719.
35 J. Moskon, M. Pivko, I. Jerman, E. Tchernychova, N. Z. Logar, M. Zorko, V. S. Selih, R. Dominko and M. Gaberscek, *J. Power Sources*, 2016, **303**, 97–108.
36 Y. Hong, Z. L. Tang, Z. J. Hong and Z. T. Zhang, *J. Power Sources*, 2014, **248**, 655–659.
37 J. H. Zheng, *Discrete Continuous Dyn. Syst. - Ser. A*, 2015, **35**, 2273–2298.
38 Y. J. Zhu and C. S. Wang, *J. Phys. Chem. C*, 2011, **115**, 823–832.
39 Y. Qian, C. Wang and F. Gao, *Biosens. Bioelectron.*, 2015, **63**, 425–431.
40 L. E. Li, J. Liu, L. Chen, H. Y. Xu, J. Yang and Y. T. Qian, *RSC Adv.*, 2013, **3**, 6847–6852.
41 Y. Qian, F. Gao, L. Du, Y. Zhang, D. Tang and D. Yang, *Biosensors and Bioelectronics*, 2015, **74**, 483–490.